

Application of Galerkin spectral method for tearing mode instability

Wu Sun(孙武), Jiaqi Wang(王嘉琦), Lai Wei(魏来), Zhengxiong Wang(王正汹),Dongjian Liu(刘东剑), and Qiaolin He(贺巧琳)

Citation: Chin. Phys. B, 2022, 31 (**11**): 110203. DOI: 10.1088/1674-1056/ac600d

What follows is a list of articles you may be interested in

Furi-Martelli-Vignoli spectrum and Feng spectrum of nonlinear block operator matrices

Xiao-Mei Dong(董小梅), De-Yu Wu(吴德玉), and Alatancang Chen(陈阿拉坦仓)

Chin. Phys. B, 2021, 30 (**4**): 040201. DOI: 10.1088/1674-1056/abd7df

Local structure-preserving methods for the generalized Rosenau-RLW-KdV equation with power law nonlinearity

Jia-Xiang Cai(蔡加祥), Qi Hong(洪旗), Bin Yang(杨斌)

Chin. Phys. B, 2017, 26 (**10**): 100202. DOI: 10.1088/1674-1056/26/10/100202

Conservative method for simulation of a high-order nonlinear Schrödinger equation with a trapped term

Cai Jia-Xiang (蔡加祥), Bai Chuan-Zhi (柏传志), Qin Zhi-Lin (秦志林)

Chin. Phys. B, 2015, 24 (**10**): 100203. DOI: 10.1088/1674-1056/24/10/100203

A conservative Fourier pseudospectral algorithm for the nonlinear Schrödinger equation

Lv Zhong-Quan (吕忠全), Zhang Lu-Ming (张鲁明), Wang Yu-Shun (王雨顺)

Chin. Phys. B, 2014, 23 (**12**): 120203. DOI: 10.1088/1674-1056/23/12/120203

A conservative Fourier pseudospectral algorithm for a coupled nonlinear Schrödinger system

Cai Jia-Xiang (蔡加祥), Wang Yu-Shun (王雨顺)

Chin. Phys. B, 2013, 22 (**6**): 060207. DOI: 10.1088/1674-1056/22/6/060207

Application of Galerkin spectral method for tearing mode instability

Wu Sun(孙武)[1], Jiaqi Wang(王嘉琦)[1,†], Lai Wei(魏来)[2], Zhengxiong Wang(王正汹)[2], Dongjian Liu(刘东剑)[1], and Qiaolin He(贺巧琳)[3]

[1] *College of Physics & Key Laboratory of High Energy Density Physics and Technology, Sichuan University, Chengdu* 610065, *China*
[2] *School of Physics, Dalian University of Technology, Dalian* 116024, *China*
[3] *School of Mathematics, Sichuan University, Chengdu* 610065, *China*

(Received 31 December 2021; revised manuscript received 15 March 2022; accepted manuscript online 23 March 2022)

Magnetic reconnection and tearing mode instability play a critical role in many physical processes. The application of Galerkin spectral method for tearing mode instability in two-dimensional geometry is investigated in this paper. A resistive magnetohydrodynamic code is developed, by the Galerkin spectral method both in the periodic and aperiodic directions. Spectral schemes are provided for global modes and local modes. Mode structures, resistivity scaling, convergence and stability of tearing modes are discussed. The effectiveness of the code is demonstrated, and the computational results are compared with the results using Galerkin spectral method only in the periodic direction. The numerical results show that the code using Galerkin spectral method individually allows larger time step in global and local modes simulations, and has better convergence in global modes simulations.

Keywords: Galerkin spectral method, tearing mode instability, magnetic reconnection, magnetohydrodynamics

PACS: 02.70.Hm, 52.35.Py, 52.35.Vd, 52.65.Kj **DOI:** 10.1088/1674-1056/ac600d

1. Introduction

Magnetic reconnection, the topological rearrangement of magnetic field lines, was proposed to explain solar flares by Giovanelli.[1] In astrophysical,[1–5] space,[6–9] and laboratory plasmas,[10–14] the phenomenon has been broadly observed, which converts the magnetic energy into thermal and kinetic energies of the plasma. Theoretically, there are two widely quoted theoretical magnetic reconnection mechanisms, namely Sweet–Parker model and Petschek model.[15,16] Magnetic reconnection is considered to play an important role in some processes, such as the solar flares,[2,17–21] the corona heating,[3] the coronal mass ejections (CMEs),[22] the magnetic substorms[23] and the disruption in tokamaks.[24,25] For solar flares, the CSHKP model is regarded as a standard model, in which the conversion of magnetic energy during the magnetic reconnection is thought to provide an origin for the released energy of solar flares.[17–20] Meanwhile, the extreme ultraviolet and x-ray observations also provide evidence of magnetic reconnection in solar flares.[21] In Earth's magnetosphere, the magnetic substorms explosively release energy from the solar wind, and magnetic reconnection at the magnetotail is considered to be responsible for the magnetic substorms.[23] Magnetic reconnection can be triggered by tearing mode instability, which results in magnetic islands as a consequence of finite resistivity. As one of the important magnetohydrodynamics (MHD) instabilities, tearing mode instability has been widely observed in toroidal plasmas. The magnetic island can be driven by the nonlinear tearing mode, and causes energy loss, crash and disruption.[25] As a catastrophic loss of plasma control in tokamaks, the disruption leads to large heat loads and mechanical stresses on surrounding structures, even causes damage to the machine.[25] Hence, it is crucial to develop the theoretical and simulation study of the tearing mode instability so that the dynamics of many related processes can be well understood. The linear and nonlinear theories of the tearing mode were developed by Furth *et al.*[26] and Rutherford.[11]

Spectral methods which originated in Ritz–Galerkin methods consist of Galerkin, tau and collocation methods.[27] The main difference between spectral methods, finite element methods and finite difference methods is that spectral methods use infinitely differentiable global functions as the trial functions to approach the solutions. The most frequently used trial functions are orthogonal polynomials. Spectral methods are global because the computation at any point depends on the information from the entire domain. The significant feature of spectral methods is that the convergence could be more rapid than any finite power of $1/N$, where N is the number of the terms in the orthogonal polynomials, while the solution is infinitely smooth.[27] Many schemes of spectral methods have been developed in the last few decades, especially in computational fluid dynamics.[27–29] Applications of spectral methods show good performance on many problems, such as compressible flows, incompressible flows, boundary layers, parallel flows and turbulence flows. For example, Serre and Pulicani proposed a high accuracy pseudospectral method for the computation of the three-dimensional Navier–Stokes

†Corresponding author. E-mail: jacky@scu.edu.cn

© 2022 Chinese Physical Society and IOP Publishing Ltd

equations inside a rotating cavity and the results have a good agreement with experimental and numerical studies.[30]

In recent years, several MHD codes have been developed, such as NIMROD,[31] XTOR,[32] and CLT,[33] which have been widely used to study tearing modes. Finite element and finite difference methods are used frequently as the discrete forms in these codes. Spectral methods are also used in periodic directions, showing a good performance. For instance, NIMROD uses a Fourier representation in the toroidal direction, while the accuracy for derivatives in that direction is increased and several numerical tasks are eased. XTOR uses it in all the angular directions, and the linear algebra is much more efficient for the same spectral content. Another 3D MHD code CLT, developed in recent years, also uses spectral methods in the ϕ direction of a cylindrical coordinate system (R, ϕ, Z). The effectiveness of these codes has been demonstrated, and many physical problems were studied by using these codes.[34–39] Hence, the applications of spectral methods are noteworthy in MHD simulations of tearing mode instability. However, it seems that spectral methods are not used as the discrete form individually. For example, XTOR uses a finite difference method in the radial, NIMROD uses a high-order finite element method in the poloidal plane, which uses spectral elements with high-order basis functions inside each element. In these codes, Fourier representations are used in one or two directions, and the computations are performed in the spectrum space and the physical space.

This paper investigates a Galerkin spectral method for simulating tearing modes based on a 2-field reduced magnetohydrodynamics (RMHD) model in two-dimensional space. The main feature of our code is that the Galerkin spectral method is used both in periodic and aperiodic directions. Thus, computations are performed in the spectrum space, and we do not need to transform polynomials into values, or vice versa. The mode analysis and filtering are also more convenient. Three cases are simulated in this paper, namely, case I, II, and III, which represent the single tearing mode, the double tearing mode and the $m = 1$ global tearing mode with a slab geometry, respectively. This paper is organized as follows. In Section 2, the physical model we used is given. We present the numerical algorithm in Section 3. Section 4 presents the simulation results and influences of using spectral methods individually. In the final section, a brief conclusion is given.

2. Physical model

In this paper, a rectangular coordinate system (x, y) is used. For the MHD instabilities, especially the finite resistivity induced tearing mode, the system can be described by the resistive MHD model. In the slab model, the plasma is assumed to be equilibrium static so that the initial plasma velocity $v_0 = 0$, and the plasma mass density ρ is invariant because the flow is incompressible. For simplicity, ρ is considered constant: $\rho = 1$. The set of fundamental equations are given as follows:[40]

$$\frac{\partial \psi}{\partial t} = [\psi, \phi] + S^{-1}\nabla_\perp^2 \psi, \tag{1}$$

$$\frac{\partial U}{\partial t} = [U, \phi] + [j_z, \psi], \tag{2}$$

where ψ, ϕ, S, U, and $j_z = -\nabla_\perp^2 \psi$ are the magnetic flux function, stream function, Lundquist number, vorticity, and z-component of current density, respectively. The functions ψ and U can be expressed as

$$\boldsymbol{B} = \nabla\psi \times \boldsymbol{e}_z, \tag{3}$$

$$\boldsymbol{U} = \nabla \times \boldsymbol{v} = -\nabla_\perp^2 \phi \boldsymbol{e}_z = U\boldsymbol{e}_z, \tag{4}$$

where $\boldsymbol{B}$ is the magnetic field, $\boldsymbol{v}$ is the plasma velocity, and the Poisson bracket is

$$[f, g] = \left(\frac{\partial f}{\partial y}\frac{\partial g}{\partial x} - \frac{\partial f}{\partial x}\frac{\partial g}{\partial y}\right). \tag{5}$$

The Lundquist number $S = \tau_\eta/\tau_\mathrm{a}$, where $\tau_\eta = \mu_0 L^2/\eta$ is the diffusion time due to the finite resistivity and $\tau_\mathrm{a} = L/v_\mathrm{a}$ is the Alfvénic time. The characteristic length L is twenty times the current sheet width, $v_\mathrm{a} = B_L/(\mu_0\rho)^{1/2}$ is the Alfvénic speed, B_L is the magnetic field at $x = L$, μ_0 is the vacuum permeability, and η is the plasma resistivity. Variables are normalized as $\boldsymbol{v}/v_\mathrm{a} \to \boldsymbol{v}$, $t/\tau_\mathrm{a} \to t$, $\boldsymbol{B}/B_L \to \boldsymbol{B}$, $\boldsymbol{E}/(v_\mathrm{a}B_L) \to \boldsymbol{E}$, $\boldsymbol{J}/(B_L/\mu_0 L) \to \boldsymbol{J}$, $\psi/(B_L L) \to \psi$, $\phi/(v_\mathrm{a}L) \to \phi$, $U/(v_\mathrm{a}/L) \to U$, and $\eta/\left(\mu_0 L^2/\tau_\mathrm{a}\right) \to \eta$, where $\boldsymbol{E}$ and $\boldsymbol{J}$ are the electric field and current density, respectively.

By asymptotic expansion method, a function f can be represented as $f(x,y,t) = f_0 + f_1(x,y,t)$, where the subscript 0 and 1 denote equilibrium quantities and perturbations, respectively. For the equilibrium quantities independent of y, we have

$$\frac{\partial f_0}{\partial y} = 0, \quad \nabla_\perp^2 f_0 = \frac{\partial^2}{\partial x^2} f_0. \tag{6}$$

Equations (1) and (2) can be written as

$$\begin{aligned}\frac{\partial \psi_1}{\partial t} = &-\frac{\partial \psi_0}{\partial x}\frac{\partial \phi_1}{\partial y} + \frac{\partial \psi_1}{\partial y}\frac{\partial \phi_1}{\partial x} - \frac{\partial \psi_1}{\partial x}\frac{\partial \phi_1}{\partial y} \\ &+ S^{-1}\left(\frac{\partial^2 \psi_1}{\partial x^2} + \frac{\partial^2 \psi_1}{\partial y^2}\right),\end{aligned} \tag{7}$$

$$\begin{aligned}\frac{\partial U_1}{\partial t} = &\frac{\partial U_1}{\partial y}\frac{\partial \phi_1}{\partial x} - \frac{\partial U_1}{\partial x}\frac{\partial \phi_1}{\partial y} + \frac{\partial}{\partial x}\left(\frac{\partial^2 \psi_0}{\partial x^2}\right)\frac{\partial \psi_1}{\partial y} \\ &+ \frac{\partial}{\partial y}\left(\frac{\partial^2 \psi_1}{\partial x^2} + \frac{\partial^2 \psi_1}{\partial y^2}\right)\left(\frac{\partial \psi_1}{\partial x} + \frac{\partial \psi_0}{\partial x}\right) \\ &+ \frac{\partial}{\partial x}\left(\frac{\partial^2 \psi_1}{\partial x^2} + \frac{\partial^2 \psi_1}{\partial y^2}\right)\frac{\partial \psi_1}{\partial y}.\end{aligned} \tag{8}$$

3. Numerical algorithm

In this MHD code, Galerkin spectral method is employed in all directions, and the 4th order Runge–Kutta scheme is used in the time-advance. The simulation domain is $(0,b)\times(0,c)$. Because Galerkin spectral method is used in all directions, computations are performed in the spectrum space.

In Galerkin spectral method, the trial functions must fit the boundary conditions, and the test functions are the same as the trial functions. In this paper, the simulation includes local modes and global modes. Fourier functions are used as the trial functions in the y direction because of the periodic boundary conditions. Different boundary conditions were assumed according to the features of local modes and global modes.

For case I, the plasma displacement of single tearing mode is localized around the rational surface,[41] thus the perfectly conducting wall boundary can be applied in the x direction. For case II, the double tearing mode can exist when two rational surfaces are close enough.[41] Away from the rational surface, the perfectly conducting wall boundary condition is still suitable for case III.

For cases I and II, half-wavelength sine series is used to fit the boundary condition, and the perturbed field can be represented as

$$\begin{aligned} f_1(x,y,t) &= \sum_{m=-\infty}^{\infty}\sum_{l=1}^{\infty} a_{m,l}\sin\left[\left(l\frac{\pi}{b}\right)x\right]\mathrm{e}^{\mathrm{i}(m2\pi/c)y} \\ &\approx f^{M,N} = \sum_{m=-N}^{N}\sum_{l=1}^{M} a_{m,l}\sin\left[\left(l\frac{\pi}{b}\right)x\right]\mathrm{e}^{\mathrm{i}(m2\pi/c)y}, \end{aligned} \tag{9}$$

where $a_{m,l}$ is the coefficient, which is also the amplitude of the corresponding Fourier (m,l) component, where m and l denote the mode numbers in y and x directions.

For case III, the feature of global mode should be considered. The $m=1$ tearing mode results in a single displacement of the flux surfaces,[42] and the perfectly conducting wall boundary is not suitable for the left boundary. Thus, the Neumann boundary $f_1'=0$ and the perfectly conducting wall boundary are used on the left and right edges of the simulation domain, respectively. Cosine series is shifted to fit the boundary condition, the series can be written as

$$f^{M,N} = \sum_{m=-N}^{N}\sum_{l=1}^{M} a_{m,l}\cos\left[\left(l-\frac{1}{2}\right)\frac{\pi}{b}x\right]\mathrm{e}^{\mathrm{i}(m2\pi/c)y}. \tag{10}$$

The approximation error estimate of Eq. (9) can be written as

$$\begin{aligned} &\|u-P_{M,N}u\|_{L^2(\Omega)} \\ &\le C_1N^{-W}\left\|u_y^{(W)}\right\|_{L^2(\Omega)} + C_2M^{-Q}\left\|u_x^{(Q)}\right\|_{L^2(\Omega)}, \end{aligned} \tag{11}$$

where u is the perturbed field in Eq. (9), $P_{M,N}u = \sum_{m=-N}^{N}\sum_{l=1}^{M} a_{m,l}[\sin(l\pi/b)x]\mathrm{e}^{\mathrm{i}(m2\pi/c)y}$, $u_y^{(W)} = \partial^W u/\partial y^W$, $u_x^{(Q)} = \partial^Q u/\partial y^Q$, C_1 and C_2 are both constant. The derivation of Eq. (11) is shown in the Appendix A and the estimate of Eq. (10) is similar. Thus, the error converges to zero when the mode number increases.

The trial functions and test functions can be chosen with above equations. In the Galerkin spectral method, equations (7) and (8) become

$$\int_0^c\int_0^b \frac{\partial\psi_1}{\partial t}\overline{f^{M,N}}\,\mathrm{d}x\mathrm{d}y = \int_0^c\int_0^b\left[-\frac{\partial\psi_0}{\partial x}\frac{\partial\phi_1}{\partial y}+\frac{\partial\psi_1}{\partial y}\frac{\partial\phi_1}{\partial x}-\frac{\partial\psi_1}{\partial x}\frac{\partial\phi_1}{\partial y}+S^{-1}\left(\frac{\partial^2\psi_1}{\partial x^2}+\frac{\partial^2\psi_1}{\partial y^2}\right)\right]\overline{f^{M,N}}\,\mathrm{d}x\mathrm{d}y, \tag{12}$$

$$\begin{aligned} \int_0^c\int_0^b \frac{\partial U_1}{\partial t}\overline{f^{M,N}}\,\mathrm{d}x\mathrm{d}y = \int_0^c\int_0^b\Bigg[&\frac{\partial U_1}{\partial y}\frac{\partial\phi_1}{\partial x}-\frac{\partial U_1}{\partial x}\frac{\partial\phi_1}{\partial y}+\frac{\partial}{\partial x}\left(\frac{\partial^2\psi_0}{\partial x^2}\right)\frac{\partial\psi_1}{\partial y} \\ &+\frac{\partial}{\partial y}\left(\frac{\partial^2\psi_1}{\partial x^2}+\frac{\partial^2\psi_1}{\partial y^2}\right)\left(\frac{\partial\psi_1}{\partial x}+\frac{\partial\psi_0}{\partial x}\right)+\frac{\partial}{\partial x}\left(\frac{\partial^2\psi_1}{\partial x^2}+\frac{\partial^2\psi_1}{\partial y^2}\right)\frac{\partial\psi_1}{\partial y}\Bigg]\overline{f^{M,N}}\,\mathrm{d}x\mathrm{d}y, \end{aligned} \tag{13}$$

where $\overline{f^{M,N}}$ is the conjugate of $f^{M,N}$, equilibrium quantities and perturbations are represented as trial functions.

With the orthogonality of the trial functions and test functions, equations (12) and (13) can be transformed to coefficient equations. Thus, the differential equations (7) and (8) can be solved in the spectrum space, and the derivations of coefficient equations are shown in the Appendix B. The coefficients of the stream function ϕ can not be obtained directly, and it is necessary to solve Poisson's equation at every time step. Fortunately, U is represented by polynomials in this paper. Thus, the Poisson's equation becomes a linear equation of the two coefficient vectors.

To compare with the Galerkin spectral method, we also implement finite difference collocation method. The code uses the finite difference method in the x direction and the Fourier-collocation method in the y direction. The computational grid is vertically divided, and each term of sine series or cosine series in the Galerkin spectral code corresponds to one node in the finite difference collocation code. In the y direction, the fast-Fourier transform (FFT) is used to transform fields to Fourier functions, where derivation is easily computed, then the inverse FFT transforms the results back into the real coordinate space. The Poisson's equation of U is solved by transforming U into a suitable function of x and y.

4. Simulation results

In this section, the simulation results of the three cases are shown. By comparing with the linear theory, the effectiveness of the Galerkin spectral code is implemented. Then the influence of using the Galerkin spectral method is discussed by comparing the results of the Galerkin spectral code with the finite difference collocation code.

4.1. Equilibrium and perturbation setting

The simulation region is $(0, 1.5) \times (0, 1)$. The set of equilibrium magnetic field is

$$B_0(x) = \tanh \frac{x - x_q}{d}, \tag{14}$$

where x_q is the peak position of the current sheet and d is the sheet width. We choose $d = 0.05$. For case I, $x_q = 0.75$. For case II, $x_q = 0.3$.

For case II, there are two current sheets, so the magnetic field is given by

$$B_0(x) = \tanh \frac{x - x_{q2}}{d} - \tanh \frac{x - x_{q1}}{d} + 1, \tag{15}$$

where x_{q1} and x_{q2} are the peak positions of two current sheets, $x_{q1} = 0.72$, $x_{q2} = 0.78$.

The initial perturbation is set as

$$\psi_1(x, y) = \tilde{\psi}_1 e^{-\left(\frac{x - x_q}{d}\right)^2} \cos(2\pi m y), \tag{16}$$

where m is the mode number in the y direction and $\tilde{\psi}_1$ is the amplitude of the initial perturbation.

The equilibrium parameter settings of case I, including the magnetic field B_0, the magnetic flux ψ_0 and the current density j_0, are shown in Fig. 1(a). As the trial functions have been chosen in Section 3, B_0 and j_0 can be transformed into truncated cosine series and sine series, respectively.

The global modes also have been simulated. If there is more than one rational surface ($\boldsymbol{k} \cdot \boldsymbol{B} = 0$) and these surfaces are sufficiently close, the double tearing mode can exist because of the drive between each rational surface.[41] Thus, the equilibrium of case II has two close current sheets, as shown in Fig. 1(b). Case III is simulated with suitable boundary conditions chosen in Section 3, and the equilibrium is plotted in Fig. 1(c).

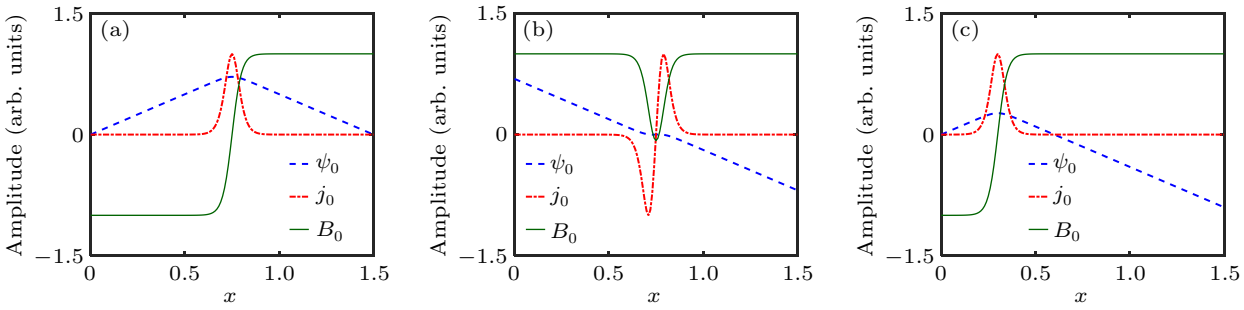


Fig. 1. Equilibrium profile of the three cases: (a) I, (b) II, and (c) III.

4.2. Mode structure

Figure 2(a) shows the mode structure of a linear single tearing mode. According to the Furth–Killeen–Rosenbluth (FKR) theory,[26] the mode is purely growing and symmetric. Priest showed the mode structure of the linear tearing mode in his paper,[24] which is in accordance with the result.

The result of case III is reported in Fig. 2(b). The $m = 1$ tearing mode in cylindrical geometry is found when the safety factor $q < 1$ at the center of the plasma, which results in a displacement of the entire plasma column instead of significant distortions of the flux surfaces.[42] The mode structure in Fig. 2(b) shows the rapid decrease of the magnetic flux in the current sheet. Thus, case III is also tested.

In Fig. 2(c), the linear result of case II is plotted, with a small surface distance. The mode structure of a large rational surface distance is shown in Fig. 2(d). As the two graphs show, the two single tearing modes developed at each corresponding rational surfaces couple with each other when they are close enough. When the distance is sufficiently large, the modes decouple, and the double tearing mode becomes two single tearing modes.

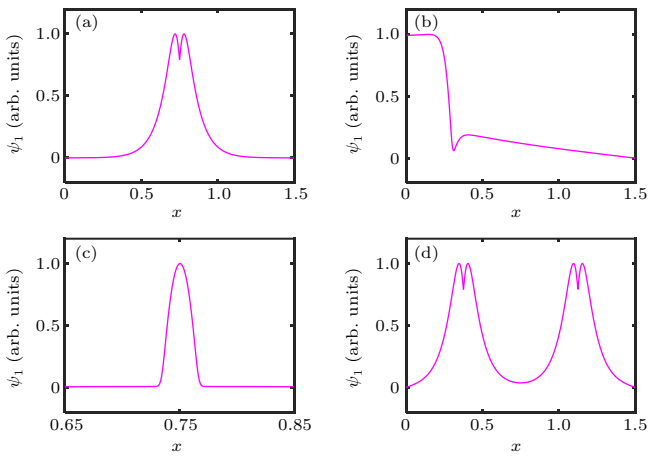


Fig. 2. Mode structures: (a) case I with $S = 10^6$, (b) case III with $S = 10^5$, (c) case II with $S = 10^6$, (d) case II with $S = 10^6$ while $x_{q1} = 0.375$ and $x_{q2} = 1.125$.

4.3. Resistivity scaling of growth rates

The growth rate scaling of the local tearing mode has been benchmarked in this part. The FKR theory[26] predicts the linear growth rate of a resistive tearing mode scaling as $\gamma \sim \tau_R^{-3/5}\tau_A^{-2/5}$. The growth rate also can be written as $\gamma \sim \eta^{3/5} \sim S^{-3/5}$. One assumption of FKR is that the flux perturbation is considered to be constant because the growth time of the mode is much longer than the skin time of the tearing layer.[41] For global modes, the assumption is invalid, and the growth rate is $\gamma \sim \eta^{1/3}$.[26,41]

The scaling benchmark of the Galerkin spectral code and the finite difference collocation code are shown in Fig. 3. The data are plotted in the double-logarithmic coordinates, and the theoretical scaling is plotted as a line. The scaling results of these two codes are in good agreement. In Fig. 3(a), the scaling of growth rates of case I is shown, and the resistivity scaling is near $S^{-3/5}$ over the range of S from 10^5 to 10^7. Figure 3(b) shows the result of case II, and the accurate range of S is from 5×10^6 to 10^7. The scaling of case III plotted in Fig. 3(c) shows that the data provides a good fit to the theory when S is near 10^5. Thus, the scaling results of the three cases are all in accordance with the theory.

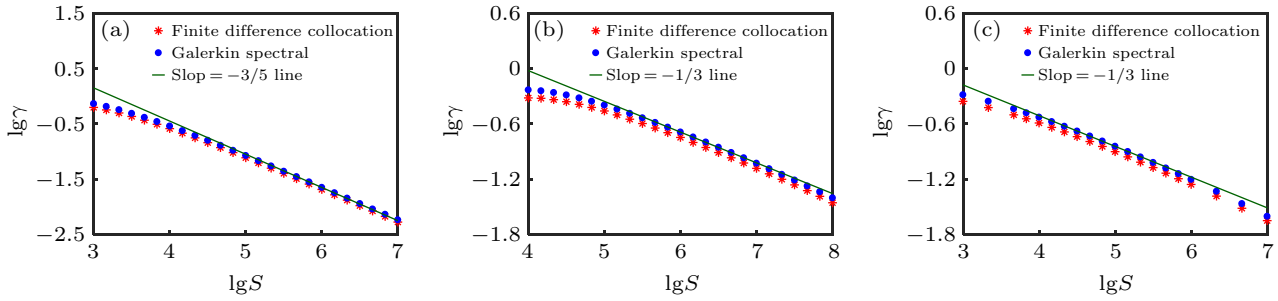


Fig. 3. Resistivity scaling of growth rates for the three cases: (a) I, (b) II, and (c) III.

4.4. Convergence benchmark

The convergence in the x direction is benchmarked in this part. As the spatial resolution increases, the data error of a numerical code should converge to zero.

Figure 4 shows the growth rate convergence of the two codes under the same spatial resolutions, while the resistivities are chosen based on the scaling result. In Fig. 4(a), the convergence rates of the two codes are similar. For case II or III, it shows a significant difference that the convergence of the Galerkin spectral code is faster compared to the finite difference collocation code. As shown in Fig. 4(b), the Galerkin spectral code reaches convergence when the number of grid points is larger than 600, while the convergence of the finite difference collocation code needs a larger grid number. For case III, the result in Fig. 4(c) reveals much difference. Thus, the simulation indicates that the Galerkin spectral code has a better performance of the convergence in global modes simulations, which shows better accuracy.

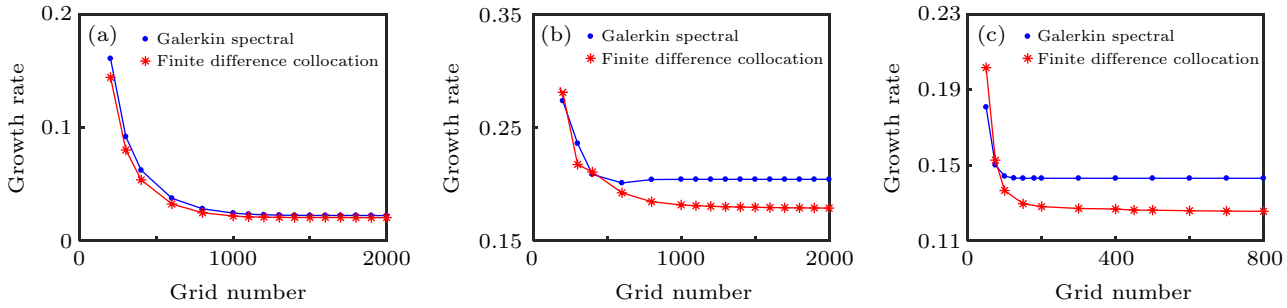


Fig. 4. Convergence comparisons: (a) case I with $S = 10^6$, (b) case II with $S = 10^6$, (c) case III with $S = 10^5$.

4.5. Stability analysis

The time step is limited by the numerical stability. Figure 5 shows the limited maximum time step of the two codes. The maximum time step Δt is compared under equal grids, and the resistivities are chosen based on the scaling result. As Fig. 5(a) shows, the results of case I and II are the same. Compared with the finite difference collocation code, the Galerkin spectral code allows larger time step at small grid number, and Δt decreases faster as the grid number increases.

As the results in Fig. 5(b), the maximum time step shows a relationship nearly $\Delta t \propto n^{-2}$ with the grid number, so further computations are performed. In Fig. 6(a), the maximum time step of case I and II with $S = 10^4$ are shown. The smaller resistivity is chosen because of less computational cost, and there is still a square relationship. The influence of the time-advance scheme is also discussed in Figs. 6(b) and 6(c), the relationships between Δt and n under different schemes are sufficiently close.

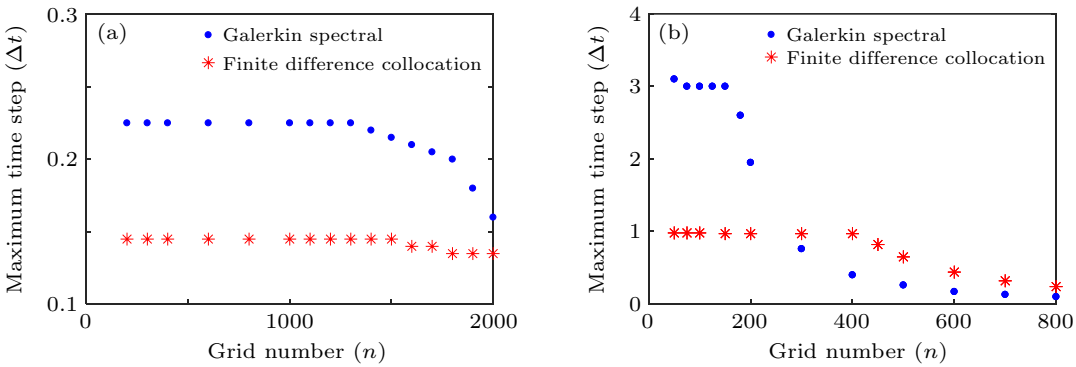


Fig. 5. Maximum time step comparisons: (a) the same result of case I and II with $S = 10^6$, (b) the result of case III with $S = 10^5$.

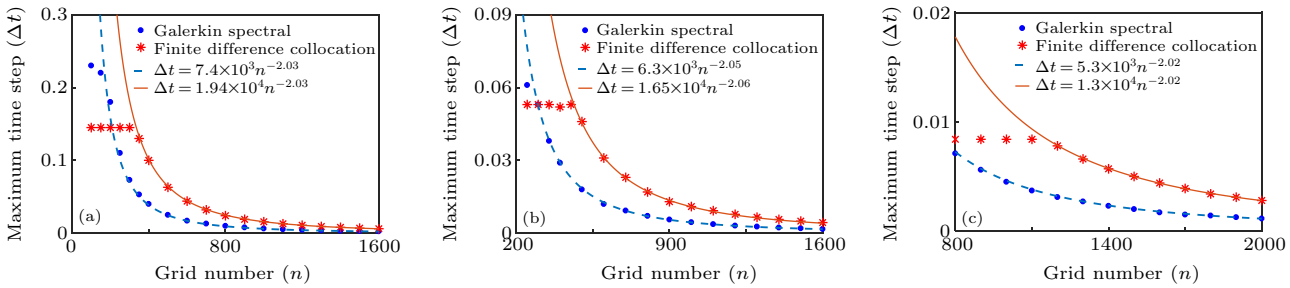


Fig. 6. Maximum time step of case I and II with $S = 10^4$: (a) 4th order Runge–Kutta method, (b) 2nd order Runge–Kutta method, (c) Euler method.

4.6. Nonlinear results

Considering the fine mode structure of tearing mode in x direction, the nonlinear simulation of the single tearing mode is performed with $-8 \le m \le 8$ and $1 \le l \le 256$. Because the boundary conditions are based on local modes, the $m = 1$ mode in this case is equal with the $m \ge 2$ modes in the cylinder geometry. The nonlinear simulation uses the same equilibrium profiles as that in case I, which is shown in Fig. 1(a). The perturbation is set as Eq. (16).

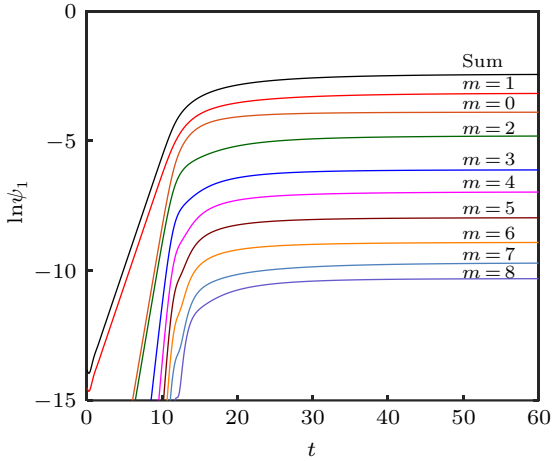


Fig. 7. Growth of magnetic flux perturbation in the current sheet.

Adopting filter in the x direction as

$$\frac{\sin(l\pi/M)}{l\pi/M}, \quad l = 1,2,\ldots,M. \tag{17}$$

The filtering is performed by altering the expansion coefficients so that the expansion coefficients decay faster for the higher l. The computation is convenient because the equations are solved in the spectrum space.

Figure 7 shows the magnetic flux perturbation, including modes from 0 to 8 and the sum of all modes. The $m = 1$ perturbation drives the increase of higher m modes, and the growth is exponential in the linear stage. As the higher harmonic grows, the nonlinear interactions between different modes become stronger, and the exponential growth is drastically slowed in the nonlinear stage. And there is nonlinear saturation in the end of the linear stage. The results are in accordance with the features of the nonlinear tearing modes.

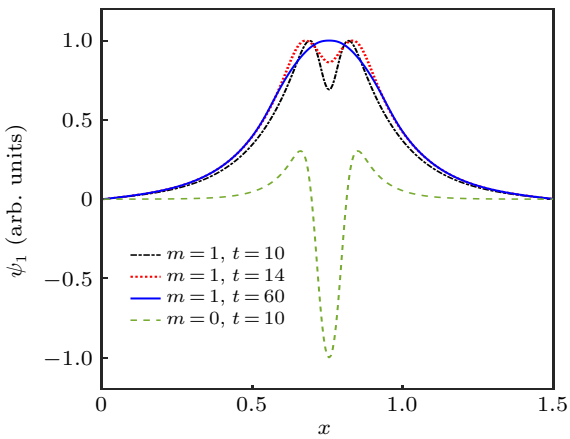


Fig. 8. Mode structures of $m = 0$ mode and $m = 1$ mode at different stages.

The mode structures are shown in Fig. 8, with $m = 1$. The unstable mode structure in the linear stage $t < 10$ is shown by a black dot, the nonlinear evolution in the later stage $10 < t < 30$ is shown by a red dash, and the saturate stage $t > 30$ is shown

by a blue solid line. The structure is a good agreement with the theory.[24] The $m = 0$ mode of magnetic flux perturbation at $t = 10$ is also plotted, showing a good agreement with the result of the previous studies.[43] Figure 9 shows the growth of the magnetic island width, and the flux perturbation is also plotted. The growth is exponential in the linear stage, then becomes linear, and tends to be zero. The saturated magnetic islands are given in Fig. 10.

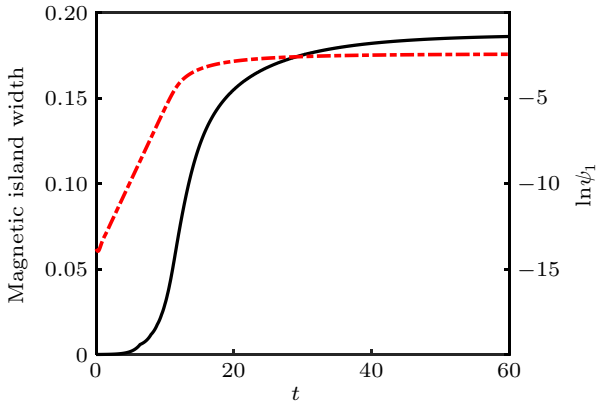


Fig. 9. Growth of magnetic island width (the black line) and perturbation of magnetic flux (the red dash line).

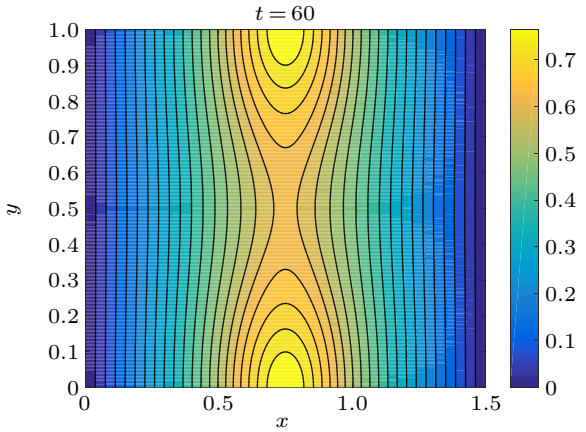


Fig. 10. Saturated magnetic islands.

5. Conclusion

A Galerkin spectral code is developed to simulate tearing modes, which is based on a 2-field RMHD model. Galerkin spectral method is used both in periodic and aperiodic directions. The partial differential equations are solved in the spectrum space, and mode analysis is more convenient in our code. In this paper, both local modes and global modes are simulated with proper boundary conditions. The trial functions are chosen to fit the boundary conditions, and the approximation error is estimated.

The linear results of local and global tearing modes, as well as the nonlinear results of local tearing mode, provide a good fit to the theory. As a comparison, the finite difference collocation code which uses spectral methods in periodic directions is developed. The resistivity scaling results of the two codes are both in accordance with the theory. Compared with the finite difference collocation code, the Galerkin spectral code shows higher accuracy of global modes. The stability analysis demonstrates that the relationship between the maximum time step Δt and the grid number n is nearly $\Delta t \propto n^{-2}$ when the grid number is sufficiently large. Although the maximum time step of the Galerkin spectral code decreases faster as the grid number increases, still keeps advantages in a range where the grid number satisfies the convergence condition. In the future work, one will generalize the code to a 3D MHD code of cylindrical geometry or toroidal geometry.

Appendix A: The estimate of approximation error

The Fourier approximation has been discussed in some references.[27,44] The computational domain is $(0,\pi) \times (0,2\pi)$. Define S_N as the space of the Fourier series, and $P_N : L^2(0,2\pi) \to S_N$ is the orthogonal projection upon S_N in the inner product of $L^2(0,2\pi)$:

$$(u - P_N u, \phi) = 0, \quad \forall \phi \in S_N, \tag{A1}$$

where $L^2(0,2\pi)$ is the space of square Lebesgue integrable functions. With the form of S_N, P_N is a truncate operator:

$$P_N\left(\sum_{m=-\infty}^{\infty} u_m \phi_m\right) = \sum_{m=-N}^{N} u_m \phi_m, \quad \phi_m \in S_N. \tag{A2}$$

With the above conditions, the estimate is

$$\|u - P_N u\|_{L^2(0,2\pi)} \le C N^{-W} \left\|u^{(W)}\right\|_{L^2(0,2\pi)}, \tag{A3}$$

where $u^{(W)}$ means the W-th order derivative of u, $W \ge 0$, C is a constant.

The estimate in two dimensions can be discussed in the following steps. First, the truncated series of u are

$$P_{M,N} u = P_N^F P_M^S u = \sum_{m=-N}^{N} \sum_{l=1}^{M} a_{m,l} \sin(lx) e^{imy}, \tag{A4}$$

where P_N^F and P_M^S represent the orthogonal projections of the Fourier series and sine series, respectively. Then we have

$$u - P_N^F P_M^S u = u - P_N^F u - \left(I - P_N^F\right)\left(I - P_M^S\right) u + u - P_M^S u, \tag{A5}$$

where I is the unit operator. Thus, the estimate in two dimensions can be obtained by Eq. (A5).

The estimate can be written as

$$\begin{aligned} \left\|u - P_N^F u\right\|_{L^2(\Omega)} &= \int_0^{\pi}\int_0^{2\pi} \left(\left|u - P_N^F u\right|^2 \mathrm{d}y\mathrm{d}x\right)^{1/2} \\ &\le C_3 N^{-W} \left\|u_y^{(W)}\right\|_{L^2(\Omega)}, \end{aligned} \tag{A6}$$

$$\begin{aligned} \left\|u - P_M^S u\right\|_{L^2(\Omega)} &= \left(\int_0^{2\pi}\int_0^{\pi} \left|u - P_M^S u\right|^2 \mathrm{d}x\mathrm{d}y\right)^{1/2} \\ &\le C_4 M^{-Q} \left\|u_x^{(Q)}\right\|_{L^2(\Omega)}, \end{aligned} \tag{A7}$$

$$\left\|\left(I-P_N^F\right)\left(I-P_M^S\right)u\right\| \le CM^{-W}\left\|\left(u-P_M^S u\right)_y^{(W)}\right\|_{L^2(\Omega)} \le C_5 N^{-W}\left\|u_y^{(W)}\right\|_{L^2(\Omega)}. \tag{A8}$$

where $Q \ge 0$, $\Omega = (0,\pi)\times(0,2\pi)$.

Thus, the estimate in two dimensions is

$$\|u-P_{M,N}u\|_{L^2(\Omega)} \le C_1 N^{-W}\left\|u_y^{(W)}\right\|_{L^2(\Omega)} + C_2 M^{-Q}\left\|u_x^{(Q)}\right\|_{L^2(\Omega)}, \tag{A9}$$

where C_1, C_2, C_3, C_4, C_5 are constants.

Appendix B: The coefficient equations

In this part, the derivations of coefficient equations are introduced. The coefficient equations can be deduced from the sample equations as follows:

$$\frac{\partial f^{M,N}}{\partial t} = L_1 g^{M,N} L_2 h^{M,N}, \tag{B1}$$

$$\frac{\partial f^{M,N}}{\partial t} = L_1 g^{M,N}, \tag{B2}$$

where L_1 and L_2 are space operators,

$$f^{M,N} = \sum_{m=-N}^{N}\sum_{l=1}^{M} a_{m,l}\varphi_l(x)\phi_m(y),$$

$g^{M,N}$ and $h^{M,N}$ are truncated series like $f^{M,N}$. The forms of L_1 and L_2 depend on Eqs. (7) and (8), $\varphi_l(x)$ and $\phi_m(y)$ are trial functions in the x direction and y direction, respectively. Equations (B1) and (B2) represent two forms of terms in the coefficient equations. In Eq. (B1), $\partial a_{m,l}/\partial t$ is relevant to coefficients of two series $g^{M,N}$ and $h^{M,N}$. And it is relevant to coefficients of series $g^{M,N}$ in Eq. (B2). The terms in Eqs. (7) and (8) correspond to the right side of Eq. (B1) or (B2).

The coefficient equations of x and y can be considered separately. In the y direction, Eqs. (B1) and (B2) can be written as

$$\int_0^{2\pi}\frac{\partial f^N}{\partial t}F^N\,\mathrm{d}y = \int_0^{2\pi} G^N H^N F^N\,\mathrm{d}y, \tag{B3}$$

$$\int_0^{2\pi}\frac{\partial f^N}{\partial t}F^N\,\mathrm{d}y = \int_0^{2\pi} G^N F^N\,\mathrm{d}y, \tag{B4}$$

where $f^N = \sum_{m=-N}^{N} a_{m_1}\phi_{m_1}(y)$, $F^N = \sum_{m=-N}^{N}\overline{\phi_m}(y)$, $G^N = L_1 g^N = \sum_{m=-N}^{N} b_{m_2} L_1\phi_{m_2}(y)$, and $H^N = L_2 h^N = \sum_{m=-N}^{N} c_{m_3} L_2\phi_{m_3}(y)$. The $\phi_{m_1}(y)$, $\phi_{m_2}(y)$, and $\phi_{m_3}(y)$ are the trial functions, and the $\overline{\phi_m}(y)$ are the test functions, where m, m_1, m_2, and m_3 are integers. The trial functions and test functions in the y direction are chosen in Section 3. Considering that $\partial_y \mathrm{e}^{\mathrm{i}my} = \mathrm{i}m\mathrm{e}^{\mathrm{i}my}$, f^N, F^N, G^N, and H^N are both the Fourier series.

With the orthogonality, the coefficient equations can be expressed as

$$\frac{\partial a_{m_1}}{\partial t} = b_{m_2}c_{m_3}, \quad m_1 = m_2 + m_3, \tag{B5}$$

$$\frac{\partial a_{m_1}}{\partial t} = b_{m_2}, \quad m_1 = m_2. \tag{B6}$$

Focus on the x direction, equations (B1) and (B2) become

$$\int_0^{\pi}\frac{\partial f^M}{\partial t}F^M\,\mathrm{d}x = \int_0^{\pi} G^M H^M F^M\,\mathrm{d}x, \tag{B7}$$

$$\int_0^{\pi}\frac{\partial f^M}{\partial t}F^M\,\mathrm{d}x = \int_0^{\pi} G^M F^M\,\mathrm{d}x, \tag{B8}$$

where $f^M = \sum_{l_1=1}^{M} a_{l_1}\varphi_{l_1}(x)$, $F^M = \sum_{l=1}^{M}\overline{\varphi_l}(x)$, $G^M = L_1 g^M = \sum_{l_2=1}^{M} b_{l_2} L_1\varphi_{l_2}(x)$, and $H^M = L_2 h^M = \sum_{l_3=1}^{M} c_{l_3} L_2\varphi_{l_3}(x)$. The $\varphi_{l_1}(x)$, $\varphi_{l_2}(x)$, and $\varphi_{l_3}(x)$ are the trial functions, and the $\overline{\varphi_l}(x)$ are the test functions, where l, l_1, l_2, and l_3 are positive integers. The trial functions of case I and II are sine series in the x direction. Considering that $\partial_x \sin lx = l\cos lx$, and $\partial_x^2 \sin lx = -l^2 \sin lx$, f^M, F^M, and G^M are sine series, and H^M are cosine series. Then the coefficient equations of the sine series can be written as

$$\frac{\partial a_{l_1}}{\partial t} = Z_1 b_{l_2} c_{l_3}, \tag{B9}$$

$$Z_1 = \begin{cases} -1/2, & l_3 = l_2 + l_1, \\ 1/2, & l_3 = l_2 - l_1 \text{ or } l_3 = l_1 - l_2, \\ 0, & \text{others}, \end{cases} \tag{B10}$$

$$\frac{\partial a_{l_1}}{\partial t} = b_{l_2}, \quad l_1 = l_2. \tag{B11}$$

Since the trial functions of case III are shifted cosine series as Eq. (10), the coefficient equations are different. For case III, the functions in Eq. (B8) are all the shifted cosine series and the result is the same as Eq. (B11). The functions G^M in the Eq. (B7) are the cosine series without phase changing, while F^M, f^M, and H^M are shifted cosine series. Thus, we have

$$\frac{\partial a_{l_1}}{\partial t} = Z_2 b_{l_2} c_{l_3}, \tag{B12}$$

$$Z_2 = \begin{cases} 1/2, & l_2 = l_3 - l_1 \text{ or } l_2 = l_1 - l_3 \text{ or } l_2 = l_3 + l_1 - 1, \\ 0, & \text{others}. \end{cases} \tag{B13}$$

The coefficient equations can be composed of the above equations.

Acknowledgments

Project supported by the Sichuan Science and Technology Program (Grant No. 22YYJC1286), the China National Magnetic Confinement Fusion Science Program (Grant No. 2013GB112005), and the National Natural Science Foundation of China (Grant Nos. 12075048 and 11925501).

References

[1] Giovanelli R G 1947 *Mon. Not. R. Astron. Soc.* **107** 338
[2] Giovanelli R G 1946 *Nature* **158** 81
[3] Tsuneta S 1996 *Astrophys. J.* **456** 840
[4] Burch J L and Phan T D 2016 *Geophys. Res. Lett.* **43** 8327
[5] Wyper P F, Antiochos S K and DeVore C R 2017 *Nature* **544** 452
[6] Dungey J W 1961 *Phys. Rev. Lett.* **6** 47
[7] Boozer A H 2012 *Phys. Plasmas* **19** 092902
[8] Angelopoulos V, Artemyev A, Phan T D and Miyashita Y 2020 *Nat. Phys.* **16** 317
[9] Phan T D, Eastwood J P, Shay M A, *et al.* 2018 *Nature* **557** 202
[10] Furth H P, Rutherford P H and Selberg H 1973 *Phys. Fluids* **16** 1054
[11] Rutherford P H 1973 *Phys. Fluids* **16** 1903
[12] Von Goeler S, Stodiek W and Sauthoff N 1974 *Phys. Rev. Lett.* **33** 1201
[13] Wang J, Xiao C, Wang X, Ji X and Liu Y 2012 *Plasma Phys. Control. Fusion* **54** 122001
[14] Kim G, Yun G S, Woo M, Park H K and the KSTAR Team 2018 *Plasma Phys. Control. Fusion* **60** 035009
[15] Parker E N 1957 *J. Geophys. Res.* **62** 509
[16] Petschek H E and Thorne R M 1967 *Astrophys. J.* **147** 1157
[17] Carmichael H 1964 *The Physics of Solar Flares, Proceedings of AAS-NASA Symposium*, 1964, Washington, D.C., USA, p. 451
[18] Sturrock P A 1966 *Nature* **211** 695
[19] Hirayama T 1974 *Sol. Phys.* **34** 323
[20] Kopp R A and Pneuman G W 1976 *Sol. Phys.* **50** 85
[21] Su Y, Veronig A M, Holman G D, Dennis B R, Wang T, Temmer M and Gan W 2013 *Nat. Phys.* **9** 489
[22] Dahlin J T, Antiochos S K and DeVore C R 2019 *Astrophys. J.* **879** 96
[23] Angelopoulos V, McFadden J P, Larson D, Carlson C W, Mende S B, Frey H, Phan T, Sibeck D G, Glassmeier K H, Auster U, Donovan E, Mann I R, Rae I J, Russell C T, Runov A, Zhou X Z and Kepko L 2008 *Science* **321** 931
[24] Priest E R 1985 *Rep. Prog. Phys.* **48** 955
[25] Wesson J 2004 *Tokamaks*, 3rd edn. (Oxford: Clarendon Press) pp. 374–390
[26] Furth H P, Killeen J and Rosenbluth M N 1963 *Phys. Fluids* **6** 459
[27] Canuto C, Hussaini M Y, Quarteroni A and Zang T A 1987 *Spectral Methods in Fluid Dynamics* (New York: Springer-Verlag) pp. 3–7, 183–278
[28] Canuto C, Hussaini M Y, Quarteroni A and Zang T A 2007 *Spectral Methods: Evolution to Complex Geometries and Applications to Fluid Dynamics (Scientific Computation)* (Berlin: Springer-Verlag) pp. 39–430
[29] Le Maître O P and Knio O M 2010 *Spectral Methods for Uncertainty Quantification: With Applications to Computational Fluid Dynamics* (New York: Springer-Verlag) pp. 107-339
[30] Serre E and Pulicani J P 2001 *Computers & Fluids* **30** 491
[31] Glasser A H, Sovinec C R, Nebel R A, Gianakon T A, Plimpton S J, Chu M S, Schnack D D and the NIMROD Team 1999 *Plasma Phys. Control. Fusion* **41** A747
[32] Lütjens H and Luciani J F 2008 *J. Comput. Phys.* **227** 6944
[33] Wang S and Ma Z W 2015 *Phys. Plasmas* **22** 122504
[34] Brennan D P, La Haye R J, Turnbull A D, Chu M S, Jensen T H, Lao L L, Luce T C, Politzer P A, Strait E J, Kruger S E and Schnack D D 2003 *Phys. Plasmas* **10** 1643
[35] Granetz R, Whyte D G, Izzo V A, Biewer T, Reinke M L, Terry J, Bader A, Bakhtiari M, Jernigan T and Wurden G 2006 *Nucl. Fusion* **46** 1001
[36] Lutjens H and Luciani J F 2010 *J. Comput. Phys.* **229** 8130
[37] Halpern F D, Lütjens H and Luciani J F 2011 *Phys. Plasmas* **18** 102501
[38] Zhang W, Wang S and Ma Z W 2017 *Phys. Plasmas* **24** 062510
[39] Zhang W, Ma Z W, Zhang H W and Zhu J 2019 *Phys. Plasmas* **26** 042514
[40] Bi H L, Wei L, Fan D M, Zheng S and Wang Z X 2016 *Acta Phys. Sin* **65** 225201 (in Chinese)
[41] Pritchett P L, Lee Y C and Drake J F 1980 *Phys. Fluids* **23** 1368
[42] Drake J F 1978 *Phys. Fluids* **21** 1777
[43] Yagi M, Yoshida S, Itoh S I, Naitou H, Nagahara H, Leboeuf J N, Itoh K, Matsumoto T, Tokuda S and Azumi M 2005 *Nucl. Fusion* **45** 900
[44] Gottlieb D and Hesthaven J S 2007 *Spectral Methods for Time-Dependent Problems* (Cambridge: Cambridge University Press) pp. 34–42